Theoretical model for the separated flow around an accelerating flat plate using time-dependent self-similarity

A. C. DeVoria [1] and K. Mohseni [1,2,*]

[1]*Department of Mechanical & Aerospace Engineering, University of Florida, Gainesville, Florida 32611, USA*
[2]*Department of Electrical & Computer Engineering, University of Florida, Gainesville, Florida 32611, USA*

(Received 30 October 2020; accepted 15 April 2021; published 10 May 2021)

We present a model appropriate to the initial motion of a flat-plate airfoil accelerating in an inviscid fluid. The model is based on the one presented in Pullin and Wang [J. Fluid Mech. **509**, 1 (2004)] and is intended to extend the range of validity to lower angles of attack and longer distances traveled. The separated flow structures are represented as vortex sheets in the conventional manner and similarity expansions locally applicable to the leading and trailing edges of the plate are developed. In our approach, an expansion is applied to the attached outer flow rather than the vortex sheet circulations and positions. This allows the asymmetric effect of the sweeping component of the free-stream flow parallel to the plate to be built in to the same governing equation as the singular-order flow. Additionally, we develop a time-dependent self-similarity procedure that allows the modeling of more complex evolution of the flow structures. This is accomplished through an implicit time variation of the similarity variables. As a collective result, the predicted vortex dynamics and forces on the plate compare favorably to Navier-Stokes simulations. The model is split into high and low angles of attack regimes. The former assumes that the leading-edge and trailing-edge flows evolve independently, while the latter makes a further simplification to couple the two flows.

DOI: 10.1103/PhysRevFluids.6.054701

I. INTRODUCTION

The two-dimensional flow around a flat-plate airfoil is a canonical problem of classical aerodynamics and has been extensively studied by theorists, experimentalists, and computationalists alike. Accordingly, it continues to serve as a benchmark for developing new, low-order inviscid modeling techniques that tackle physical problems with increasing complexity. In particular, a myriad of methods have been proposed for the vortex shedding from both the leading and trailing edges and the corresponding unsteady forces exerted on the plate, for example Refs. [1–12]. Many of these studies have been motivated by biological flows, such as flapping and hovering bird flight and fish locomotion, in which the propulsive appendage and/or the animal itself usually performs an oscillatory motion characterized by large incidences. Despite the rather disparate Reynolds number regimes of the physical and modeled problems, e.g., $\mathrm{Re} \sim O(10) - O(10^3)$ vs $\mathrm{Re} \to \infty$, the force predictions from the inviscid flow have achieved impressive accuracy. The implication is that pressure forces due to normal stress dominate in the massively separated flows.

Pullin and Wang [1] approached the problem of separated flow from the edges of a flat-plate airfoil using perturbation expansions of the singular-order similarity solutions for the separated flow around a semi-infinite flat plate (i.e., with no intrinsic length scale) as computed by Pullin [13]. Expansions of both the vortex sheet positions and circulations were carried out in the small

*mohseni@ufl.edu

parameter $\epsilon(t) = \sqrt{R_v(t)/c}$, where $R_v(t)$ is the time-dependent length scale appropriate to the size of the growing vortex spiral and c is the chord length of the plate. Recently, Sohn [12] used the same approach to include rotation of the plate. Interestingly, rotation does not change the fundamental form of the asymptotic equation as the effect can be embedded within $R_v(t)$, which is known *a priori* to the solution.

The objective of Pullin and Wang [1] was to capture the effect of asymmetry due to the sweeping component of the free-stream flow parallel to the plate. Again, this was implemented through higher-order corrections to the sheet positions and circulations, with the expectation that subsequent corrections to the forces on the plate would be obtained. This led to a series of ordered integrodifferential equations to be solved in succession, the first being the singular-order equation of Pullin [13]. The approach was successful for the former quantities. However, due to the construction of the expansions, the higher-order corrections to the vortex force vanished through cancellations. Nevertheless, at high angles of attack their force prediction performed fairly well since the wake structure approaches symmetry as the plate becomes normal to the free-stream flow. As the incidence was decreased, the prediction worsened. Similarly, for increasing time the predicted forces began to deviate from computational results after about 0.5–1 chords of travel for incidences below 60°.

Chen, Colonius, and Taira [14], inspired by the work of Pullin and Wang, conducted a computation study to more thoroughly investigate the effect of airfoil acceleration on the formation of the leading-edge vortex (LEV). Additionally, their low Reynolds number Navier-Stokes simulations, $\mathrm{Re} \sim O(10^2)$, were carried out to large times, beyond the applicability of Pullin and Wang's model, in order to characterize the full range of transient features of the vortex shedding. In particular, they found that the early-time lift peak due to the LEV only became prominent for angles of attack above about 30° and the lift augmentation lasted for about 4.5 chords of travel. However, it was noted that if the Reynolds number was to be increased, then these lower angles of attack would likely display similar lift histories. This highlights the Reynolds-number-dependent gray area of when leading-edge separation occurs and forms an organized LEV.

In lieu of continuous vortex sheets, it is common to use point vortices to represent the shed vorticity. However, the flow separation at the leading edge (LE) has presented difficulties to such models at moderate angles of attack. This has called into question the efficacy of the leading-edge Kutta condition as an appropriate criterion to produce reliable flow simulations. To address these issues, point vortex models often employ some *in situ* criteria to control the position, velocity, and/or strength of newly shed vortices [2,6,7,11,15,16]. The most promising of these remedies is the leading-edge suction parameter (LESP) criterion developed by Ramesh *et al.* [16], which suppresses vortex shedding at the LE until a critical LESP value is exceeded. The physical reasoning behind the LESP is that a finite-thickness airfoil can support some amount of suction as the flow navigates around the (rounded) leading edge without separating. Then, above the critical LESP, the rollup of the separated flow is reasonably well captured by the release of discrete point vortices that are now "shielded" from a destructive interaction with the free-stream flow. Of particular note, Ramesh *et al.* [16] showed that, in absence of reversed flow, the critical LESP is insensitive to the motion kinematics and is only a function of the airfoil shape and operating Reynolds number. As such, the critical LESP can be calibrated from a single simulation or experiment and used generally for arbitrary kinematics. Recently, Hirato *et al.* [17] demonstrated the successful extension of the LESP concept to finite wings.

For a more thorough summary of the current understanding and future prospect of research on LEVs, the reader is referred to the recent review by Jones and Eldredge [18]. This collective work presents experimental, computational, and low-order modeling results for two-dimensional airfoils in translation and pitching, as well as for finite-aspect-ratio wings with translating and rotating and revolving kinematics.

The *a priori* knowledge of the critical LESP value is required to close the problem, as it replaces the LE Kutta condition in determining the amount of vorticity released from that edge. As such, the ensuing flow evolution and dynamics predicted by an inviscid model implicitly depend on the

critical LESP. As an alternative, Darakananda *et al.* [10] have taken to estimating this value using a data assimilation approach. In this method, the critical LESP is taken as an unknown in the system of equations, which are augmented by real-time measurements of the airfoil surface pressure obtained from a "truth" simulation. The pressure data are used to inform a dynamic value of the critical LESP, which can be a function of time and is more adept to handle disturbances such as gusts or wing maneuvers.

In this paper, we aim to extend the high angle of attack vortex sheet model of Pullin and Wang [1] to lower incidences and longer chord lengths traveled. Our approach is similar, but does not employ an infinite-term perturbation series for the sheet positions and circulations. Instead, under certain conditions to be identified in this paper, the asymmetric sweeping effect can be brought into the same order as the singular attached flow around the edges. The result corresponds to the expansion of the attached outer flow to higher order. In essence, a new singular-order governing equation is obtained that includes the asymmetry, but which is only trivially altered from the integrodifferential equation that governs the singular-order flow alone.

The extended model consists of two tiers or angle of attack regimes. In the moderate-to-high incidence range, a well-formed separated LEV structure is present. More specifically, in this range the initial developments of the LEV and trailing-edge vortex (TEV) are assumed to be independent of each other. However, in the low-to-moderate incidence range the sweeping component of the free stream is too strong to consider the TEV development as independent of the flow near the leading edge. Instead of a separated LEV, the leading-edge flow is returned to the singular attached flow, which is then coupled to the TEV evolution through the governing equation.

The remainder of the paper is organized as follows. In Sec. II we discuss the expansion of the outer attached flow around a sharp wedge that will eventually be applied near the leading and trailing edges of the flat plate. The full problem statement of the flow around the plate is given in Sec. III. This is followed by the derivation of the self-similar approximation and solution for the higher angle of attack regime in Sec. IV, which is then adapted to the lower angle of attack regime in Sec. V. Section VI presents applied results of our model as well as comparisons to Navier-Stokes simulations.

II. OUTER FLOW EXPANSION

In this section we briefly introduce the concept that will ultimately serve as the basis for our model of the flow around the flat plate. Any analytic function, such as the complex potential, can be expanded in a convergent Laurent series about a point z_o that consists of positive and negative powers of $(z - z_o)$, which correspond to outer and inner expansions, respectively [19]. If the function is also analytic at the point z_o itself, then the series becomes the more familiar Taylor series. The outer expansion represents the effect of distant agencies; "Moffatt eddies" [20] are a well-known flow induced by such phenomena. Conversely, the inner expansion corresponds to local (i.e., singular) agencies; for example, the vorticity field associated with a moving contact line has a dipole distribution [21].

In the particular case of flow around a sharp wedge of interior angle $\beta\pi$ $(0 \leqslant \beta < 1)$ with apex located at $z = 0$ (see Fig. 1 for geometry), the complex potential of the attached flow can be written as [22]

$$W_a(z, t) = A_0(t) + A_1(t)z^n + A_2(t)z^{2n} + \cdots + A_k(t)z^{kn} + \ldots, \tag{1}$$

where $n = 1/(2 - \beta)$ and while W_a is finite at $z = 0$, it is not analytic since its complex derivative does not exist there. Also note that (1) has set to zero the higher-order singularities of the inner expansion corresponding to $k < 0$ terms. This expansion is assumed to be valid near the apex at small times after the onset of motion. As such, the series is usually truncated after $k = 1$ since this yields the dominating, singular term in the velocity expression dW_a/dz of this attached flow. Hence, the physical geometry reintroduces an inner expansion term of fractional power $-(1 - n)$ into the velocity. Pullin [13] regularized this flow by allowing separation at the apex to shed a self-similar

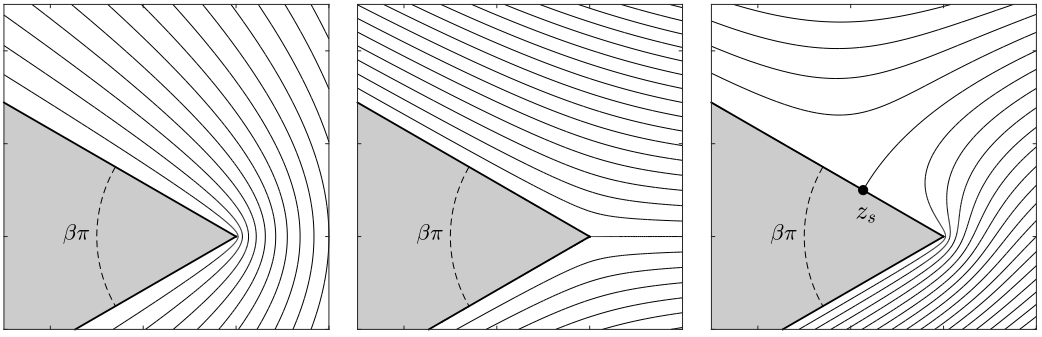

FIG. 1. Example streamlines of attached flows around a wedge of angle $\beta\pi$: (a) singular flow from bottom to top, (b) higher-order regular flow from left to right, and (c) the composite flow of Eq. (2). In (c) the black dot marks the stagnation point z_s on the wedge surface.

conventional vortex sheet. Those solutions are sometimes used as an initial condition to begin inviscid simulations with arbitrary unsteadiness (e.g., Refs. [4,12]). In DeVoria and Mohseni [22] we significantly augmented the solution space by considering an entrainment boundary condition (in place of no throughflow) that allows a complex coefficient $A_1 \in \mathbb{C}$ and the shedding of a vortex-entrainment sheet [23].

In this paper, we adopt the standard zero-entrainment boundary condition of no throughflow. However, we consider the higher-order terms in the expansion (1). Since $\frac{1}{2} \leqslant n < 1$, the $k \geqslant 2$ terms are regular at the apex, each having a defined derivative there, and again represent the outer expansion due to distant agencies. For simplicity, we truncate the series after $k = 2$ and to satisfy zero entrainment on the wedge faces, where $\arg\{z^n\} = n\theta = \pm\pi/2$, we write $A_1 = -ia$ and $A_2 = b \in \mathbb{R}$. Also, A_0 can be set to zero without affecting the attached flow velocity field, which becomes

$$\frac{dW_a}{dz} = nz^{n-1}\{-ia + 2bz^n\}. \tag{2}$$

As mentioned in Ref. [22], the higher-order terms in (1) introduce additional topological features. In the case of (2), the regular flow opposes the singular flow on one wedge face and contributes to it on the other face, and so a hyperbolic stagnation point z_s appears on the surface of opposing flows at a radial distance from the apex of

$$r_s = \left|\frac{a}{2b}\right|^{1/n}, \tag{3}$$

where z_s is on the upper surface if $a/(2b) > 0$ and on the lower surface if $a/(2b) < 0$. Figures 1(a)–1(c) show examples of the attached flow streamlines for the singular, regular, and composite flows. The radius r_s is a length scale intrinsic to the composite flow and evidently indicates the "proximity" of the distant agency of strength b to the apex where the potential of strength a dominates. In Sec. IV we will show that Eq. (2) yields the asymptotic outer flow near the leading and trailing edges of a flat plate ($n = \frac{1}{2}$) of chord length c that is translating with velocity $U(t)$ at an angle of attack α. More specifically, we will find that $a = c^{1/2}U \sin\alpha$ and $b = U \cos\alpha$, and that r_s indicates the interaction of the leading-edge and trailing-edge flows with the sweeping component of the free stream, namely, $b = U \cos\alpha$.

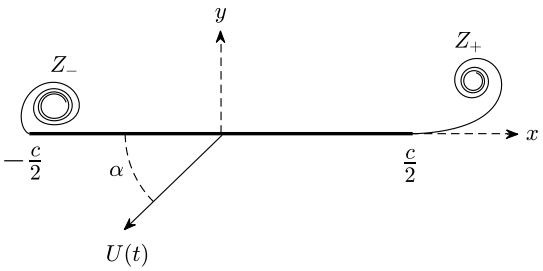

FIG. 2. Definition of the x-y coordinate system instantaneously coinciding with the mid-chord of the flat plate that translates with speed $U(t)$ and angle of attack α. The trailing edge is at $x = c/2$, while the leading edge is at $x = -c/2$. The complex positions of the corresponding shed vortex sheets are Z_+ and Z_-.

III. FLAT-PLATE AIRFOIL

Here, we give the problem formulation for the general flow around a plate that translates with speed $U(t)$ at constant angle of attack α. In the inertial frame with the fluid at rest at infinity, the plate motion is to the left and downward with velocity $U_b + iV_b = -U(t)e^{i\alpha}$ as shown in Fig. 2. As usual, the flat-plate geometry with chord length c in the physical plane, where $z = x + iy$ is the complex coordinate, is obtained from the mapping of a circular boundary with radius $c/4$ in a virtual ζ plane via the Joukowski transformation:

$$\zeta(z) = \tfrac{1}{2}(z + \sqrt{z^2 - c^2/4}). \tag{4}$$

The origin of the coordinate system instantaneously coincides with the mid-chord of the plate so that its trailing and leading edges are located at $z = +c/2$ and $-c/2$, respectively. The vortex sheets shed from each edge have corresponding positions $Z_\pm$ in the physical plane and $\zeta_\pm = \zeta(Z_\pm)$ in the virtual plane.

Next, we give the expression for the total complex potential W_o that describes the flow. The scalar potential is ϕ and the stream function is ψ, both of which satisfy the Laplace equation in the fluid domain Ω_f with appropriate boundary conditions.

A. Complex potential

The total complex potential W_o only exists in the analytic region Ω_f, i.e., the fluid domain, that is outside the plate and any sheets of discontinuity shed from the plate. Let the contour immediately surrounding these inner boundaries be $C_i \in \Omega_f$. Since the spatial domain is two dimensional, then a discontinuity in W_o may also exist due to a logarithmic constituent and requires a branch cut C_{cut} to be specified so that the logarithm is uniquely defined. The cut intersects the plate at a point $z_c(t)$ and must extend to infinity where it connects to an all-enclosing contour C_∞. Each side of C_{cut} is a distinct portion of the fluid boundary. This ensures that W_o is single valued in the simply connected region defined by the *complete* fluid boundary $\partial\Omega_f = C_i + C_{\text{cut}} + C_\infty$. Therefore, all the usual statements regarding the properties of analytic functions apply in the region Ω_f (e.g., see Refs. [19,24,25]).

The real and imaginary parts of the jump in W_o (due to the logarithm) across the cut respectively correspond to the net circulation $\Gamma_o(t)$ around and the net flux $Q_o(t)$ across a contour C_o that encloses the plate and any shed sheets [23]. As a consequence of the Cauchy-Goursat theorem, we must have $\Gamma_o = \Gamma_i = \Gamma_\infty$, where Γ_i and Γ_∞ are the circulations around the (closed) contours C_i and C_∞, respectively. In other words, the arbitrary closed contour C_o is reconcilable within the (topologically) annular region between C_i and C_∞, and thus the circulation around any such contour is Γ_o. Analogous statements can be made about the flux Q_o.

The quantities Γ_o and Q_o must be specified as input, or otherwise determined, to have a unique solution for the complex potential. Since we have imposed the normal boundary condition of zero entrainment everywhere on the inner boundary C_i, then $Q_o \equiv 0$ necessarily. In the case of a flow started from rest (when the fluid is free of discontinuities), Kelvin's circulation theorem is usually invoked to arrive at the result that $\Gamma_o(t) \equiv 0$. It is often taken for granted that this result requires the assumptions that C_o does not, at any time, intersect a discontinuity in velocity nor pressure, and that no nonconservative forces $\boldsymbol{f}$ (with $\boldsymbol{\nabla} \times \boldsymbol{f} \neq \boldsymbol{0}$) act tangentially anywhere along the contour. Such nonconservative forces acting on the portion of C_i that coincides with the plate surface could be used to model vorticity generation. While we will not explore the physical details of any of these circulation-generating mechanisms in this study, we will carry through the analysis with $\Gamma_o(t) \neq 0$ for general posterity.

The total circulations in the shed sheets Z_+ and Z_- are Γ_+ and Γ_-, respectively, while the "bound" circulation around the plate is Γ_b. Accordingly, the circulation around the arbitrary contour C_o enclosing the entire plate and sheet system is $\Gamma_o = \Gamma_b + \Gamma_+ + \Gamma_-$. In general, so long as the boundary $\partial\Omega_f$ is known along with the value of W_o on $\partial\Omega_f$, then a unique solution exists for W_o with a given value of Γ_o and without requiring any further information about the bound or vortex sheet circulations. However, we assume that the vortex sheets emanate from the edges of the plate on the physical basis that the velocity remains finite there. Hence, two more relations are required to ensure that this is indeed satisfied. These supplemental constraints are the Kutta conditions and are sufficient to determine the individual circulations Γ_+ and Γ_-, and since Γ_o will be known from the dynamics (via Kelvin's theorem), then Γ_b is obtained as well. This completes the unique determination of the complex potential and we may now state its analytic expression.

The total complex potential can be written as $W_o = W_b + W_+ + W_-$, where W_b and $W_\pm$ are the contributions from the plate and the shed vortex sheets. Let $W_\infty = -zUe^{-i\alpha}$ be the potential of a moving reference frame translating with the plate. By the circle theorem [26], the plate potential W_b can be represented in closed form in this noninertial frame by the image systems of $W_\pm$ and W_∞. The resulting expression for this relative complex potential defined as $W \equiv W_o - W_\infty$ is

$$W = W_a + W_v + \frac{\Gamma_o}{2\pi i}\log\zeta, \tag{5a}$$

$$W_a = zU\,\cos\alpha - iU\,\sin\alpha\sqrt{z^2 - c^2/4}, \tag{5b}$$

$$W_v = \frac{1}{2\pi i}\sum_{\pm}\int_0^{\Gamma_\pm}[\log(\zeta - \zeta_\pm) - \log(\zeta - \zeta_\pm^i)]d\Gamma, \tag{5c}$$

where W_a is the potential of the attached flow, W_v is the potential due to the vortex system and includes the contributions from the sheets in the fluid as well as their corresponding images located at $\zeta_\pm^i = (c/4)^2/\overline{\zeta}_\pm$; an overbar denotes the complex conjugate. Here and elsewhere, the sum is shorthand for the addition of the integrals with terms respectively having $(+)$ and $(-)$ subscripts. The logarithmic constituent is the image of the net circulation Γ_o at infinity, which here can be written explicitly as the uniformly valid term $\log\zeta$ via the circle theorem. This circulation does not affect the kinematics represented by the normal boundary condition on the plate (Neumann problem). In fact, it is the single remaining degree of freedom in the *tangential* boundary condition (Dirichlet problem), which represents the dynamics. As mentioned above, the physical principle used to fix the value of Γ_o is Kelvin's theorem. Having specified the flow solution, next we discuss the expression for the force exerted on the plate.

B. Force on the plate

The force on the plate is computed as the integral of pressure around its surface. Since the vortex sheets are assumed to have a zero pressure jump, then the integral can be augmented to include those sheets and thus the contour replaced by that of the inner boundary C_i. Following Newman [27] and

temporarily using vector notation, this pressure integral can be rewritten to give the force as

$$F = \rho \frac{d}{dt} \oint_{C_i} \phi \hat{\boldsymbol{n}}\, dl + \rho \oint_{C_\infty} \left[\frac{1}{2} |\boldsymbol{u}|^2 \hat{\boldsymbol{n}} - \boldsymbol{u}(\boldsymbol{u} \cdot \hat{\boldsymbol{n}}) \right] dl. \tag{6}$$

From here, there are two different ways to proceed, the details of which depend on the reference frame; the end result is the same, of course. In the *moving* frame, the C_∞ integral yields the familiar Joukowski force associated with Γ_o (see Batchelor [28]). In the *stationary* frame the integral vanishes, but the Joukowski force reappears from the time derivative of the logarithmic constituent of ϕ in the C_i integral, which we discuss next.

In either frame, due to the zero-entrainment boundary condition, the scalar potential in (6) can be replaced by the complex potential. Generally, an integral of the stream function ψ is also present, but which is proportional to the fluid mass displaced by the body [29], and so is zero for the flat plate. Opting for the moving frame, the residue theorem can be used to replace C_i with C_∞ for W_a and W_v in Eq. (5a). For the log term of W, however, we must use the more general Cauchy-Goursat theorem (from which the residue theorem derives) that involves the complete fluid boundary. Thus, the replacement contour includes the cut $C_\infty + C_{\text{cut}}$, and it is easy to show that the integral of $(\Gamma_o/2\pi i) \log \zeta$ over this contour evaluates to $\Gamma_o z_c$, where again z_c is the position where the cut intersects the plate. In the stationary frame, with coordinates $\tilde{z}$ and $\tilde{\zeta}$ say, the same result is obtained since the logarithm becomes $\log(\tilde{\zeta} - \tilde{\zeta}_o)$, where $\tilde{\zeta}_o(t)$ is the position of the plate mid-chord. However, the time derivative of z_c in this frame is $dz_c/dt + (-U e^{i\alpha})$ and the Joukowski force is recovered from the latter term. The first term is the velocity of $z_c(t)$ on the plate surface in the moving frame.

Returning to complex variables, we then decompose the total force as

$$F_t + iF_n = \underbrace{F_t^{(v)} + iF_n^{(v)}}_{\text{vortex force}} + \underbrace{F_t^{(b)} + iF_n^{(b)}}_{\text{body force}}, \tag{7a}$$

where for each force constituent $F_t^{(\cdot)}$, $F_n^{(\cdot)}$ are the components tangential and normal to the plate, respectively. The "vortex force" is due to W_v and the "body force" combines the contributions from W_a and Γ_o, and these are expressed by the following:

$$F_t^{(v)} + iF_n^{(v)} = i\rho \frac{d}{dt} \left\{ \sum_{\pm} \int_0^{\Gamma_\pm} (\zeta_\pm - \zeta_\pm^i)\, d\Gamma \right\}, \tag{7b}$$

$$F_t^{(b)} + iF_n^{(b)} = i\rho c^2 \frac{\pi}{4} \frac{dU}{dt} \sin\alpha + i\rho \frac{d}{dt}(z_c \Gamma_o) + i\rho \Gamma_o (-U e^{i\alpha}). \tag{7c}$$

The conventional definitions of the lift and drag forces are $D + iL = (F_t + iF_n)e^{-i\alpha}$. Next, we briefly examine a revealing connection between the plate force and the dynamics of the shed vortex system.

C. Inviscid vortex dynamics and impulse invariant

For an inviscid fluid of infinite extent there are flow invariants associated with integrals of the vorticity field [28,30] that represent the net amounts of vorticity [or circulation in two dimensions (2D)], impulse, and kinetic energy. Here, we are interested in the delivery of impulse to the fluid. For our problem the fluid remains irrotational and the effect of vorticity is represented by vortex sheets, which are boundaries to the fluid domain. As such, the impulse delivered to the fluid is equal to that of the freely shed vortex sheets. Moreover, since these sheets do not support a pressure jump, then the *net fluid impulse* can only be increased (or decreased) by an increment (or decrement) delivered by the plate, i.e., only if it accelerates.

In the case that $\Gamma_o \equiv 0$, then from (7c) we see that the plate can only deliver a net impulse in the direction normal to itself and therefore the vortex force in (7b) (due to the impulse of the shed vortex

system) will only generate a nonzero plate-normal component. This means that the plate-tangential forces of the leading- and trailing-edge vortex systems must mutually cancel by the movement and circulation dynamics of each sheet. This is despite any visual asymmetry of the total vortex system. These claims will be validated in Sec. VI with numerically computed solutions.

IV. HIGH ANGLE OF ATTACK MODEL

We are now in the position to derive approximate governing equations for solutions that are valid near the edges of the plate. Here, we discuss the moderate-to-high angle attack range, for which a well-formed LEV and TEV are both present. The main assumption is that the initial developments of the LEV and TEV are independent of each other.

First, we write the vortex sheet locations $Z_\pm$ and the total circulations $\Gamma_\pm$ as

$$Z_+ = \frac{c}{2}(1 + 2\epsilon^2\omega_+), \qquad \Gamma_+ = J_+ G, \tag{8a}$$

$$Z_- = -\frac{c}{2}(1 + 2\epsilon^2\overline{\omega}_-), \qquad \Gamma_- = -J_- G, \tag{8b}$$

where $\omega_\pm$ are the corresponding nondimensional self-similar shape functions, and again $\epsilon^2 = R_v/c$. Note the complex conjugate of ω_- defining Z_- in (8b). Also, $J_\pm$ are the nondimensional circulation *magnitudes* with $G(t)$ as the temporal growth of the circulation scaling. Further requirements of similarity restrict the plate velocity to be of the form

$$U(t) = Bt^m, \tag{9}$$

where m is given; we shall call this quantity the acceleration exponent. We refer the reader to Refs. [13,22] for more details on the self-similar problem setup. It can be shown that the velocity induced by one vortex sheet on the other at the opposing edge is of the same order as terms that we eventually will ignore and is therefore neglected now. Next, we give some detail on the case of the trailing-edge sheet Z_+, for the results applicable to the leading-edge sheet Z_- follow immediately with minor changes.

The velocity field is obtained by differentiating (5a) with respect to z and using $dW/dz = (d\zeta/dz)dW/d\zeta$ where appropriate. When $z \to Z_+$ and $\zeta \to \zeta_+$ the result becomes the Birkhoff-Rott equation $\partial\overline{Z}_+/\partial t = dW/dz$, which is the (kinematic) governing equation for the sheet. A careful expansion in ϵ of the right-hand side yields

$$\frac{dW}{dz} = \frac{\dot{R}_v}{C_o}\left[\frac{1}{2\sqrt{\omega_+}}\left\{-i\left[1 + \frac{\Gamma_o}{\pi c U \sin\alpha}\right] + (2\epsilon\ \cot\alpha)\sqrt{\omega_+} + \frac{J_+}{2\pi i}I_0(\omega_+)\right\}\right.$$
$$\left. + \epsilon\frac{J_+}{2\pi i}\{I_0(\omega_+) - I_1(\omega_+)\}\right], \tag{10a}$$

where $C_o = \epsilon\dot{R}_v/(U\ \sin\alpha)$ and

$$I_0(\omega) = \int_0^1 \left[\frac{1}{\sqrt{\omega} - \sqrt{\omega'}} - \frac{1}{\sqrt{\omega} + \sqrt{\overline{\omega}'}}\right]d\lambda', \tag{10b}$$

$$I_1(\omega) = \int_0^1 \frac{1}{2\sqrt{\omega}}\left[\frac{\omega - \omega'}{(\sqrt{\omega} - \sqrt{\omega'})^2} - \frac{\omega - \overline{\omega}'}{(\sqrt{\omega_+} + \sqrt{\overline{\omega}'_+})^2}\right]d\lambda', \tag{10c}$$

where $\lambda = 1 - \Gamma/(JG)$ is the dimensionless circulation similarity variable along the sheet and $G(t) = \epsilon c U\ \sin\alpha$; a prime indicates a dummy variable for integration. Next, substitution of (8a) into the left-hand side of the governing equation gives

$$\frac{\partial\overline{Z}_+}{\partial t} = \dot{R}_v\left[\overline{\omega}_+ + Q(1-\lambda)\frac{d\overline{\omega}_+}{d\lambda}\right], \tag{11}$$

with $Q = (4m + 1)/(2m + 2)$. This equation has no explicit $O(\epsilon)$ term since we did not consider a series expansion of Z_+. At first glance, it seems we must then neglect all of the $O(\epsilon)$ terms in (10a). However, we note that the angle of attack, which is an independently specified parameter, appears in combination with ϵ in the $2\cot\alpha$ term. Therefore, we impose the constraints

$$\epsilon \ll 1, \quad 2\epsilon\cot\alpha \equiv \eta_\alpha \sim O(1), \tag{12}$$

and drop the terms in the second set of curly brackets in (10a). The physical limitations implied by the constraints in (12) require more comment, which will be taken up shortly in Sec. IV A where the range of validity is discussed. The $2\cot\alpha$ term represents the asymmetric sweeping effect and can be found in the $O(\epsilon)$ equation of Pullin and Wang [1]. From (10a) and (2) we readily see that the attached flow terms (with $\Gamma_o = 0$) yield $a = c^{1/2}U\sin\alpha$ and $b = U\cos\alpha$ as stated in Sec. II.

Equation (11) remains unchanged from Refs. [1,13,22], and following those works we take $C_o = \frac{1}{2}$. Next, we write $\Gamma_o = J_o(\pi cU\sin\alpha)$ so that J_o is the fraction of the steady-state circulation of classical aerodynamics. We note that since $\epsilon(t)$ is a function of time, then so too is $\eta_\alpha(t)$, and likewise for $J_o(t)$ due to $\Gamma_o(t)$ and $U(t)$. As such there is a separate, implicit timescale in the physical domain solution as $Z_+(\Gamma, t) = c/2 + c\epsilon^2(t)\omega_+(\lambda, \eta_\alpha(t), J_o(t))$ and $\Gamma_+(t) = G(t)J_+(\eta_\alpha(t), J_o(t))$. We will utilize this to construct a more complex evolution of the flow structures; the procedure for this task will be further explained shortly.

The nondimensional governing equation for ω_+ is given by equating (10a) and (11), then applying (12). The equation for the leading-edge sheet ω_- is obtained from the same equation, but with $\eta_\alpha \to -\eta_\alpha$ and $J_o \to -J_o$. In this case, the solution can be transformed to the physical leading-edge location by (8b). Regarding the physical significance of η_α, we need only consider positive values, which correspond to a positive angle of attack relative to the left-to-right uniform flow in the axes fixed on the plate. On the other hand, J_o may take either sign in accordance with the sign of Γ_o. As such, we finally obtain the governing equations for $\omega_\pm$ as

$$\overline{\omega}_\pm + Q(1-\lambda)\frac{d\overline{\omega}_\pm}{d\lambda} = \frac{1}{\sqrt{\omega_\pm}}\left\{ -i(1 \pm J_o) \pm \eta_\alpha\sqrt{\omega_\pm} + \frac{J_\pm}{2\pi i}I_0(\omega_\pm)\right\}, \tag{13}$$

where the integral $I_0(\omega)$ is given by (10b). Note that the $(\pm)$ signs are taken individually for ω_+ and ω_-, respectively, and no summation is implied. The corresponding Kutta conditions at each edge are

$$0 = (1 \pm J_o) + \frac{J_\pm}{2\pi}I_0(0). \tag{14}$$

Upon specification of J_o and η_α, the equations can be solved for $\omega_\pm$ and $J_\pm$. In particular, when $\eta_\alpha = J_o = 0$, (13) reduces to the equations numerically solved by Pullin [13] and thus inclusion of nonzero values of these parameters requires only minor amendment. We use the numerical scheme described in DeVoria and Mohseni [22], which studied cases of nonzero entrainment in the starting-flow separation over sharp wedges.

Once the self-similar solutions have been computed for a given pair of η_α and J_o, they can be transformed to physical solutions using (8a) and (8b) with the following scalings:

$$\epsilon(t) = \left[C_p\left(\frac{Ut}{c}\right)\sin\alpha\right]^{1/3}, \qquad G(t) = \frac{c^2\epsilon^4}{tC_p}, \tag{15}$$

where $C_p = 3/[4(1 + m)]$ is a constant for given m. The transformation process is detailed by the flow chart in Fig. 3. As mentioned earlier, the result will include the implicit timescale contained in the parameters η_α and J_o, which represent two separate asymmetric effects. A given trajectory or curve in the η_α-J_o similarity space (parametrized by time) is obtained by beginning from the baseline and incrementing the values along the curve using the previous solution as an initial condition to the governing Eq. (13). We used an analogous procedure in Ref. [22] to represent a time-dependent shedding angle of a vortex-entrainment sheet separating from a noncusped wedge.

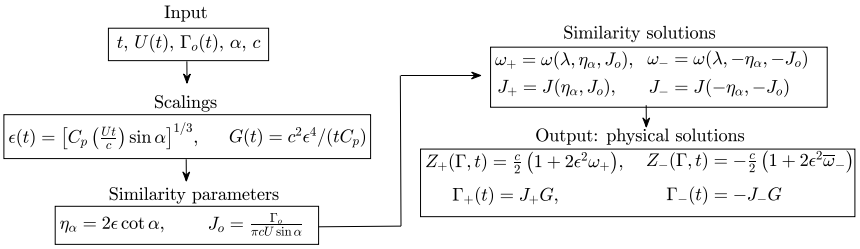

FIG. 3. Flow chart detailing the transformation of the self-similar solutions to the physical space for given input data. The similarity parameters are given to the governing equation in (13) with an appropriate initial condition.

We note that there are several useful ways to express the scaling $G(t)$, some of which are

$$G(t) = \epsilon cU\ \sin\alpha = cU\left[\frac{\epsilon^4}{C_p\left(\frac{Ut}{c}\right)}\right] = \frac{R_v^2}{tC_p} = \frac{R_v\dot{R}_v}{C_o} = \frac{\dot{G}R_v}{Q\dot{R}_v}, \tag{16}$$

where $C_o = \frac{1}{2}$. Lastly, the vortex sheet model represented by (13) and (14) requires a somewhat involved numerical solution. As such, it is worthwhile to obtain an approximate, yet more tractable solution in which the entirety of the rolled-up sheet is represented by a concentrated point vortex. This is given in the Appendix for the interested reader.

A. Range of validity

Here, we discuss how the constraints in (12) relate to the range of validity of the approximate governing equation in (13). To do so we must interpret the meaning of the similarity variable $\eta_\alpha(t) = 2\epsilon(t)\cot\alpha$. In short, this nondimensional parameter "collapses" the effects of angle of attack and the time growth of the vortex spirals. It is akin to the similarity variable for the Blasius boundary layer that collapses the viscous layer growth with downstream distance. Since $\epsilon(t) \sim t^{(m+1)/3}$, then increasing time tracks with an increase of η_α, while increasing α decreases η_α. Recall that when $\eta_\alpha = 0$, then (13) returns the singular-order equation of Pullin [13]. That same equation is also the $\epsilon(t) \to 0$ limit of Pullin and Wang's model [1], which they showed to be valid for large angles of attack. In other words, we can expect that solutions to (13) with $\eta_\alpha \ll 1$ will be similarly valid for large incidences. This is confirmed in the Appendix by comparison of their point vortex solution with the one corresponding to our model (see Fig. 13).

To consider the validity of our model for lower, yet still moderate, angles of attack, we must address the $O(\epsilon)$ integral term in (10a) that was neglected: $\epsilon\{I_0(\omega) - I_1(\omega)\}$. This represents the higher-order effect of the self-induced velocity of the vortex sheet and its image. On the other hand, the term that we retained, that is η_α, represents the higher-order effect of the attached outer flow and is technically of the same order. This is why there are two conditions in (12), which can be combined to provide an estimate of the lower limit as $\tan\alpha \approx 2$ or $\alpha \approx 63^\circ$. However, if it happens that $|I_0(\omega) - I_1(\omega)| \ll 1$ regardless of ϵ, then the lower limit of the angle of attack range can be reduced further. Unfortunately, there is no straightforward way to assert this possibility at this stage, but it can be assessed *a posteriori* by comparison of numerical solutions with viscous simulations. This task is taken up in Sec. VI B, where it is shown that the model provides fair predictions for incidences down to $\alpha = 30^\circ$ and for about 2 to 3 chords of travel.

The same type of *a posteriori* analysis could be used to investigate even lower angles of attack. However, in this case the assumption that a well-formed LEV exists and whose development remains independent from that of the TEV is no longer valid and must be revised. To this end, in Sec. V we adapt the current model by representing the leading-edge flow as a bound circulation that is mutually coupled to the TEV evolution.

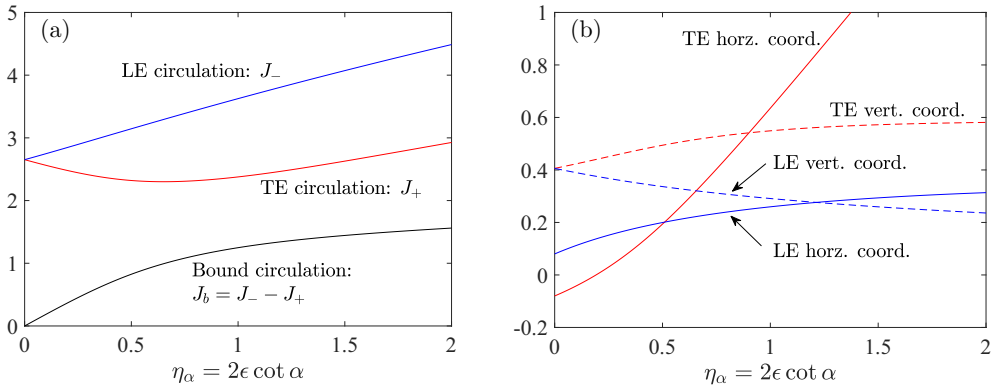

FIG. 4. Variation of similarity results with η_α for trailing-edge (+) and leading-edge (−) solutions. The parameters are $m = 0$ (impulsive acceleration) and $J_o = 0$. (a) Nondimensional circulation magnitudes in the sheets and the bound circulation. (b) Horizontal and vertical coordinates of the vortex spiral core locations for each sheet [also see Fig. 5(a)].

B. Similarity results

In this section we present results from a set of self-similar solutions to (13) corresponding to a simple combination of the similarity parameters, namely, varying η_α with $J_o = 0$. We will see that the significant effect of asymmetry is indeed captured. Physical airfoil solutions will be discussed in Sec. VI.

Figure 4(a) plots the nondimensional circulation magnitudes of the LEV and TEV sheets J_- and J_+, respectively, for the case of an impulsively accelerated plate $m = 0$. The constant acceleration case $m = 1$ displays the same trends, albeit with different quantitative values. For the LEV sheet, the circulation increases with η_α, while it initially decreases for the TEV sheet. The major advantage of our model is that nonlinear dependence on η_α comes built in with the similarity solutions $J_\pm$ and $\omega_\pm$ since the parameter η_α appears explicitly in the governing Eq. (13). For example, as seen in Fig. 4(a), a reversal in the growth trend of the TEV circulation J_+ occurs for η_α above about 0.75. Conversely, the model of Pullin and Wang [1] is a linearization at $\eta_\alpha = 0$ (see the Appendix). Also shown in Fig. 4(a) is the nondimensional bound circulation on the plate, which is given by $J_b = J_- - J_+$ since $J_o = 0$. The dimensional bound circulation is $\Gamma_b = |\Gamma_-| - \Gamma_+ > 0$ and so is in opposite sense to that of the leading-edge sheet. This quantity is one indicator of the asymmetry in the total vortex structure.

The asymmetric effects are best observed in the LEV and TEV sheet shapes. Some examples are plotted in Fig. 5 for different values of η_α and acceleration exponents m. The downstream convection of the trailing-edge (TE) spiral and the pronounced ellipticity of the LE spiral are familiar features. As the LEV grows in strength [recall Fig. 4(a)], the spiral core is pinned closer to the plate surface representing the attachment known to increase the lift [31]. To give a better idea of the "rate" at which the LE and TE spiral cores convect downstream, Fig. 4(b) plots their positions as a function of η_α for the $m = 0$ case.

C. Vortex force

In this section we perform some manipulations on the vortex force in order to obtain a more intuitive expression. Replacing Γ with the nondimensional circulation parameter λ as the integration variable in (7b) allows the vortex force to be rewritten as

$$F_t^{(v)} + iF_n^{(v)} = i\rho \frac{d}{dt}\left\{\sum_{\pm} \Gamma_\pm \left[c \int_0^1 \frac{(\zeta_\pm - \zeta_\pm^i)}{c}\, d\lambda\right]\right\} \equiv i\rho \frac{d}{dt}\left\{\sum_{\pm} \Gamma_\pm [cI_\pm]\right\}, \tag{17}$$

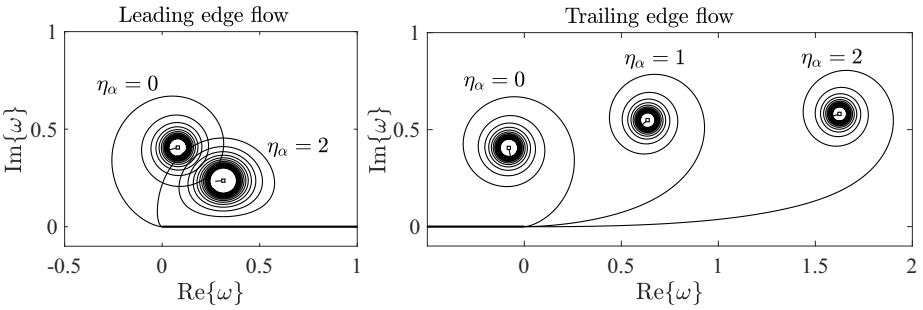

(a) Impulsive acceleration: $m = 0$

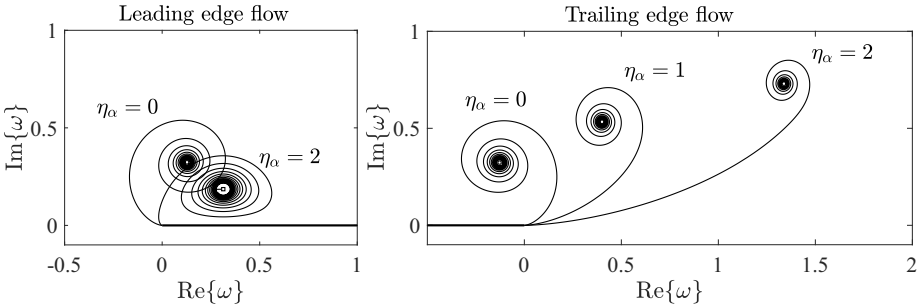

(b) Constant acceleration: $m = 1$

FIG. 5. Sheet shapes in similarity space for flow near the leading edge $-\overline{\omega}_-$ (left plots), and flow near the trailing edge ω_+ (right plots). Solutions with $J_o = 0$ and different values of the parameter $\eta_\alpha = 2\epsilon \cot\alpha$ are plotted as labeled, where $\eta_\alpha = 0$ is the baseline with no effect of asymmetry. The sweeping motion of the free-stream represented by η_α is from left to right. (a) Impulsive acceleration: $m = 0$, and (b) constant acceleration: $m = 1$.

where $I_\pm(t, \eta_\alpha, J_o)$ are symbols for the nondimensional integrals above, which depend on time explicitly as well as implicitly through the parameters η_α and J_o. The quantities $cI_\pm$ can be interpreted as the positions of point vortices with circulations $\Gamma_\pm$ that preserve the force contribution on the plate due to each vortex sheet. While we have gained higher-order effects of asymmetry by absorbing ϵ into the nondimensional governing equation through η_α, the physical positions $Z_\pm$ of the sheets given by (8a) and (8b) are still only $O(\epsilon^2)$ accurate. As such, our calculation of (17) should be of the same order. This is accomplished by substituting $Z_\pm$ into (4) to obtain $\zeta_\pm$ and these expressions into $I_\pm$, and then expanding the result for small ϵ.

First, however, a brief comment regarding the calculation of the force contribution from the LEV Z_- is appropriate. Since (8b) involves the negative conjugate of ω_-, then this operation must also be applied to the normal vector of the sheet to keep the force components consistent with the coordinate system of the problem. Also, the minus sign reflecting $\Gamma_- < 0$ is canceled (i.e., made positive) by the opposite direction of integration along the leading-edge sheet as compared to the trailing-edge sheet. In effect, the force from Z_- can be calculated in the same way as that from Z_+ and then applying the negative conjugate operation.

Returning to our task, expanding (17) and dropping terms $O(\epsilon^3)$ and higher yields

$$F_t^{(v)} + iF_n^{(v)} = \rho \frac{d}{dt}\{c\epsilon G[\epsilon(J_- T_- - J_+ T_+) + i(J_+ N_+ + J_- N_-)]\}, \tag{18a}$$

$$N_\pm = \int_0^1 \mathrm{Re}\{\sqrt{\omega_\pm}\}\, d\lambda, \qquad T_\pm = \int_0^1 \mathrm{Im}\{\omega_\pm\}\, d\lambda, \tag{18b}$$

where $N_\pm(\eta_\alpha, J_o)$ will give rise to $O(1)$ plate-normal forces and $T_\pm(\eta_\alpha, J_o)$ to $O(\epsilon)$ plate-tangential forces. If the expansions used by Pullin and Wang [1] are substituted it is found that $(J_- T_- - J_+ T_+) = 0$ and so the remaining force is normal to the plate. However, as explained in Sec. III C, this must necessarily be the case since the plate only delivers a net normal impulse to the fluid when $\Gamma_o = 0$. One will also find that $(J_+ N_+ + J_- N_-) = 2J_0 N_0$, where J_0 and N_0 are the values corresponding to the singular-order problem of Pullin [13], and thus we also recover their result that higher-order corrections to the (normal) vortex force vanish by cancellation. The cancellation occurs due to "mirror symmetries" inherent to the construction of their expansions. For our model this does not happen because the asymmetry is built in at the level of the differential equation and is propagated through to $\omega_\pm$ and $J_\pm$. Note that so long as the sheets remain above the plane of the plate, then $N_\pm > 0$ and $T_\pm > 0$. In this case, the LEV and TEV work together to produce the normal force, whereas they work against each other in establishing any tangential force.

Now, in distributing the time derivative through each term of (18a) we must account for both the explicit time dependence of $G(t)$ and $\epsilon(t)$, as well as the implicit time dependence of $J_\pm$, $N_\pm$, and $T_\pm$ via their dependence on $\eta_\alpha(t)$ and $J_o(t)$. This involves several applications of chain and product rule differentiation and results in a cumbersome expression. To maintain notational clarity we introduce an operator $\mathcal{F}_p(\mathcal{X})$ with argument $\mathcal{X}$ and parameter p that is defined by

$$\mathcal{F}_p(\mathcal{X}) \equiv \left[\left(Q + \frac{1}{p}\right)\mathcal{X} + \frac{1}{2}\eta_\alpha \frac{d\mathcal{X}}{d\eta_\alpha}\right] + J_o \frac{d\mathcal{X}}{dJ_o}\left[\frac{R_v}{\dot{R}_v}\left(\frac{\dot{\Gamma}_o}{\Gamma_o} + \frac{\dot{U}}{U}\right)\right]. \tag{19}$$

An overdot indicates time differentiation and note that $\mathcal{F}_p$ is a linear operator. Also, the second grouping of terms vanishes entirely if either $\Gamma_o = 0$ or J_o is constant; it is assumed that $U \neq 0$ for $t > 0$. The vortex force in (18a) can then be expressed as

$$F_t^{(v)} + iF_n^{(v)} = \rho c \epsilon \dot{G} Q^{-1}\{\epsilon \mathcal{F}_1(J_- T_- - J_+ T_+) + i\mathcal{F}_2(J_+ N_+ + J_- N_-)\}. \tag{20}$$

Moreover, using (15) and (16) we have

$$\rho c \epsilon \dot{G} Q^{-1} = \frac{1}{2}\rho U^2 c\left[\frac{\epsilon^5}{\left[C_p\left(\frac{Ut}{c}\right)\right]^2}\right] = \frac{1}{2}\rho U^2 c\left[\frac{\sin^{5/3}\alpha}{\left[C_p\left(\frac{Ut}{c}\right)\right]^{1/3}}\right] \sim t^{(5m-1)/3}, \tag{21}$$

thus providing a convenient form suitable to typical definitions of nondimensional force coefficients using the dynamic pressure and chord length. Although the time dependence of the force scaling in (21) is $t^{(5m-1)/3}$, it must be recalled that the nondimensional terms within the curly brackets of (20) have an implicit time dependence that is obtained from the numerical solution. Also note that $Ut/c = (1+m)(s/c)$ where $s(t)$ is the distance traveled by the plate at time t and so s/c is the number of chords traveled. The force scaling given in Ref. [1] can be recovered by substituting for $U = Bt^m$ and introducing their definitions of $K = C_p^{2/3}$ and $a = c^{1/2}B \sin\alpha$.

V. LOW ANGLE OF ATTACK MODEL

As mentioned previously, the assumption of a well-formed LEV that is independent of the TEV becomes invalid at low incidences. Again, this is because the free stream becomes more aligned with the plate chord and so increases the sweeping component of that flow. Here, we give the adaptation of our model appropriate to low angles of attack. The separated LEV sheet Z_- is not explicitly represented and is replaced with the attached singular flow around that edge. The circulation of the LEV Γ_- is lumped with the bound circulation around the plate Γ_b to give the *effective bound circulation* [32] as $\Gamma_{\text{eff}} = \Gamma_- + \Gamma_b$. Figure 6 depicts the flow configuration for this situation. The effective bound circulation is represented as a logarithmic constituent in the complex potential, which now becomes

$$W = W_a + W_v + \frac{\Gamma_o + \Gamma_{\text{eff}}}{2\pi i}\log\zeta, \tag{22}$$

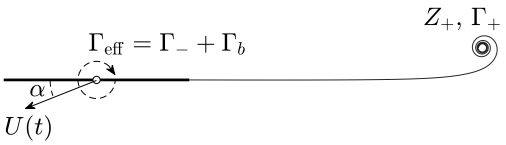

FIG. 6. Schematic of the low angle of attack range. The separated LEV sheet is neglected, but its circulation Γ_- is lumped with Γ_b to give the effective bound circulation Γ_{eff}.

where W_a is still given by (5b) and W_v by (5c) but with only the contribution from the TEV sheet Z_+. As discussed at the end of Sec. III A, the presence of the logarithmic constituent does not affect the normal boundary condition and is a degree of freedom in the tangential boundary condition. Stated differently, the circle theorem [26] as applied to vortex elements is unique up to an arbitrary circulation at the center of the cylinder.

To this end, the net circulation around the plate and TEV is $\Gamma_o = \Gamma_{\text{eff}} + \Gamma_+$ and Kelvin's circulation theorem again provides an additional equation to relate these circulations. Going forward, we employ the usual result from Kelvin's theorem for flows started from rest, namely, $\Gamma_o \equiv 0$, and so $-\Gamma_{\text{eff}} = \Gamma_+$. As in (8a), we let the nondimensional TEV circulation be $\Gamma_+ = J_+ G$, where again $G = \epsilon c U \sin\alpha$. Fortunately, the governing equations in Sec. IV are unaffected in form by our changes, and we have already done all the necessary derivation work. The only remaining issue is to address the term in (10a) from the logarithmic constituent of (22) that now corresponds to Γ_{eff}. This term becomes

$$G_{\text{eff}} \equiv \frac{-\Gamma_{\text{eff}}}{\pi c U \sin\alpha} = \frac{\epsilon J_+}{\pi} = \eta_\alpha \tan\alpha \, \frac{J_+}{2\pi}. \tag{23}$$

The appearance of $\epsilon = \sqrt{R_v/c}$ in the middle equation represents the length-scale coupling of the developments of the TEV and effective bound circulations as the vortex structures grow in time. The rightmost equation in (23) expresses the circulation in terms of our existing similarity variable η_α. This allows the flow near the trailing edge to "feel" the induced velocity of Γ_{eff}. With this, the nondimensional governing equation for the TEV sheet ω_+ and the corresponding Kutta condition are

$$\overline{\omega}_+ + Q(1-\lambda)\frac{d\overline{\omega}_+}{d\lambda} = \frac{1}{\sqrt{\omega_+}}\left\{ -i + \eta_\alpha\sqrt{\omega_+} + \frac{J_+}{2\pi i}[I_0(\omega_+) - \eta_\alpha \tan\alpha] \right\}, \tag{24a}$$

$$0 = 1 + \frac{J_+}{2\pi}[I_0(0) - \eta_\alpha \tan\alpha]. \tag{24b}$$

Again, the integral $I_0(\omega)$ is given by (10b). Unfortunately, the consequence of coupling the LE and TE flows is that Eqs. (24) explicitly contain the angle of attack. This is a disadvantage as compared to (13) whose solutions (for a given m) can be applied to any incidence. Nevertheless, the above equations are no more difficult to solve. Moreover, we note that the point vortex model in the Appendix can be applied by replacing J_o with G_{eff} from (23).

At the initial instant $\eta_\alpha = 0$ and (24) is the same as (13) with $J_o = 0$. As time and thus $\eta_\alpha > 0$ increase, the TEV and effective bound circulations develop in a coupled manner. Eventually, the TEV will shed downstream and Γ_{eff} becomes largely responsible for satisfying the Kutta condition, which now contains η_α. We therefore expect that the solutions to (24) will yield results similar to Wagner's theory [33], which makes the assumptions of a flat vortex sheet that travels downstream with the translation speed of the airfoil.

A. Force of the effective bound circulation

Since we have represented the effective bound circulation as a logarithmic constituent in the complex potential (22), then there is a force associated with Γ_{eff}, say $F_t^{(\text{eff})} + iF_n^{(\text{eff})}$, that is

analogous to the part of the body force in (7c) due to Γ_o. Here, the plane is cut along the plate and TEV sheet (see Fig. 6) so that the branch cut of the logarithm intersects the plate at the trailing edge $z_c = c/2$. Recalling that $\Gamma_{\text{eff}} = -\Gamma_+$ we then have

$$F_t^{(\text{eff})} + iF_n^{(\text{eff})} = i\rho\left\{\Gamma_+ U e^{i\alpha} - \frac{c}{2}\frac{d\Gamma_+}{dt}\right\}. \tag{25}$$

This is *not* the "circulatory" or vortex force of the TEV which is still given by (20) with only $\mathcal{F}_2(J_+N_+)$ making a contribution. Li and Wu [34] arrived at a similar, small-angle approximation of (25) [see Eq. (C11) on p. 212 of their paper].

The first term in (25) corresponds to the familiar Kutta-Joukowski lift. The second term represents the change of effective bound circulation, i.e., the tangential boundary condition. This force is analogous to the added mass, which is the other part of the body force in (7c) that is due to the normal boundary condition, but contributes no net circulation. Combining (25) with the added mass gives the total body force. Recognizing that $\Gamma_+ = \pi c U \sin\alpha G_{\text{eff}}$, then the corresponding drag and lift of the body force $D^{(b)}$ and $L^{(b)}$ can be expressed as

$$D^{(b)} = \frac{1}{2}\rho c U^2\left[\pi C_n^{(b)} \sin^2\alpha\right], \tag{26a}$$

$$L^{(b)} = \frac{1}{2}\rho c U^2\left[2\pi \sin\alpha G_{\text{eff}} + \pi C_n^{(b)} \cos\alpha \sin\alpha\right], \tag{26b}$$

$$C_n^{(b)} = \frac{c}{2U^2}\left[\frac{dU}{dt} - 2\frac{d}{dt}(U G_{\text{eff}})\right], \tag{26c}$$

where $C_n^{(b)}$ quantifies the combined added mass and $d\Gamma_+/dt$ forces. The angle of attack scalings for the $C_n^{(b)}$ terms are the same as the potential and vortex normal forces in the leading-edge suction analogy of Polhamus [35].

VI. APPLIED RESULTS

This section presents time-dependent results of our model that are converted from the similarity space to the physical space via the transformation procedure depicted in Fig. 3. To validate and exhibit the capabilities and limitations of the current inviscid model, we make comparison to different theories and viscous simulations. The net circulation Γ_o is set to zero and so $J_o = 0$ as well. Due to the familiarity of the small incidence regime, we begin in Sec. VI A with the assessment of the adaptation of our model given by (24) of Sec. V. Likewise, Sec. VI B then assesses the application of the model in (13) of Sec. IV for the moderate-to-high angle of attack range.

A. Regime I: Low-to-moderate angle of attack

For the low-to-moderate angle of attack regime, we compare to the models of Wagner [33] and Graham [3]. Wagner's quasisteady theory is for impulsive motions to steady speeds, i.e., $m = 0$, at low angles of attack. The main assumptions are that the TEV sheet remains flat and is convected downstream with the instantaneous speed of the airfoil. Graham's model accounts for the rollup of TEV sheet, but is decoupled from the leading-edge flow (much like the high-incidence form of our model given in Sec. IV). As such, Graham's model is only valid for small times and does not asymptote to a steady state like Wagner's theory.

The shed TEV circulation from Wagner's theory can be written as $\Gamma_w(t) = \Gamma_\infty G_w(\tau)$, where $\Gamma_\infty = \pi c U \sin\alpha$ is the steady-state value and $G_w(\tau)$ is the Wagner function for circulation and is a function of the "convective time" $\tau = Ut/c$. We use the empirical formula for $G_w(\tau)$ given by Li and Wu [34] [see Eq. (C3) on p. 211 of their paper]. The circulation function analogous to G_w for

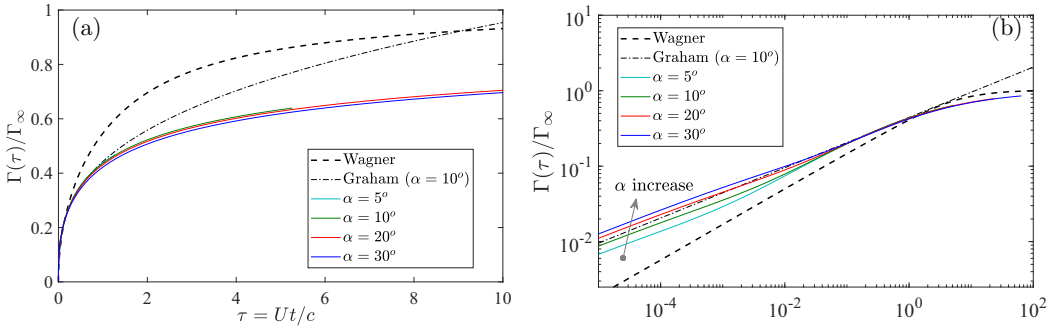

FIG. 7. (a) The circulation functions for the low angle of attack model (solid) compared with the theories of Wagner [33] (dashed) and Graham [3] (dashed-dotted) for steady translation $m = 0$. (b) The same data on a log-log scale. $\Gamma_\infty = \pi cU \sin\alpha$ is the theoretical steady-state value.

our model is the quantity G_{eff} from (23), which can also be expressed as

$$G_{\text{eff}}(\tau) = \frac{J_+(\tau)}{\pi}[C_p\tau \sin\alpha]^{1/3}. \tag{27}$$

The circulation function for Graham's theory [3] is equivalent to (27) with $J_+ = \pi(2C_p)^{-1/3}$ for all τ. Figure 7(a) plots the circulation functions for each model. For small α, we note that $\tau \sim \alpha^2\eta_\alpha^3/6$ and so fairly large values of η_α are required to make $\tau = Ut/c \approx 1$. We computed solutions up to $\eta_\alpha = 10$ for each angle of attack shown: $\alpha = 5^\circ, 10^\circ, 20^\circ, 30^\circ$. For Graham's model only a representative case of $\alpha = 10^\circ$ is shown for clarity. On this linear scale, all models agree for very small times, but the Wagner circulation function continues a faster rate of increase for $\tau > 0.25$. Unlike Graham's theory, our model has negligible dependence of G_{eff} on the angle of attack. This is because of the coupling to the leading-edge flow, and (27) implies that $J_+ \propto (\sin\alpha)^{-1/3}$. Figure 7(b) plots the same cases, but on a log-log scale. For $\tau \ll 1$ our model matches the $\tau^{1/3}$ behavior predicted by Graham's theory that accounts for the initial TEV rollup, and we can infer that $J_+(\tau) \to$ const in the same limit. For $\tau \gg 1$ our model has $G_{\text{eff}} \to 1$ agreeing with the Wagner circulation, and we can similarly infer that $J_+ \sim \pi(C_p\tau \sin\alpha)^{-1/3}$ at large times. Conversely, Graham's circulation eventually exceeds the steady-state value Γ_∞ and becomes unbounded.

The near collapse of the curves for different α in our model qualitatively agrees with Wagner's universal function. However, there is a quantitative offset that is likely related to the different assumptions of the two models, particularly the distribution of the shed vortex sheet strength. To better assess these differences, we now compare the lift force. The lift from Wagner's theory can be written as $L_w(\tau) = L_\infty\Phi_w(\tau)$, where $L_\infty = \rho\pi cU^2 \sin\alpha$ and $\Phi_w(\tau)$ is the normalized Wagner lift function. A formula for $\Phi_w(\tau)$ is also given in Li and Wu [34]. Figure 8(a) plots $\Phi_w(\tau)$ and the normalized lift for our model. Wagner's quasisteady theory does not explicitly account for the rate of change of bound/shed circulation. This is most evident from the familiar nonzero lift at $\tau = 0$ (equal to half of L_∞). The dynamic consequence of the change in the effective bound circulation is an infinite force at the initial instant (out of frame), a feature that was also predicted by Graham [3]. However, Graham's lift (not shown) becomes infinitely positive as $\tau^{-1/3}$ due to the vortex force (20), whereas in our model the vortex force is outpaced by the $d\Gamma_{\text{eff}}/dt = -d\Gamma_+/dt < 0$ term in (25). From (26c) and the small-time behavior $G_{\text{eff}} \sim \tau^{1/3}$, this force becomes infinitely negative as $\tau^{-2/3}$. The Wagner lift effectively "collapses" the short-lived time interval within which $d\Gamma_{\text{eff}}/dt$ provides an appreciable contribution to the lift. Also shown in Fig. 8(a) are some viscous simulations (Re = 500) presented in Jones and Eldredge [18]. Although there are some agreeable features, the presence of vortex shedding becomes evident around $Ut/c = 1.5$ and represents a degree of coupling that is beyond the scope of our current model.

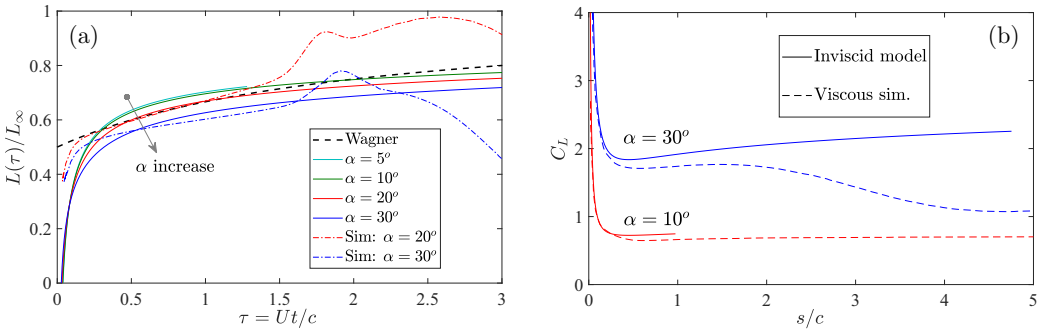

FIG. 8. (a) The lift functions for the low angle of attack model (solid) compared with the theory of Wagner [33] (dashed) and the viscous simulations (Re = 500) in Jones and Eldredge [18] (dashed-dotted) for steady translation $m = 0$. $L_\infty = \rho\pi cU^2 \sin\alpha$ is the theoretical steady-state value. (b) The modeled lift coefficient C_L (solid) versus chords traveled s/c for an accelerating plate with $m = 0.5$ for $\alpha = 10^\circ$ (red) and $\alpha = 30^\circ$ (blue). The viscous simulations (Re = 100) are from Chen, Colonius, and Taira [14] (dashed).

The examples just discussed correspond to impulsive acceleration to a steady translation, i.e., $m = 0$. Now, we briefly assess the model for a continually accelerating plate with $m = 0.5$. Figure 8(b) plots the lift coefficient, defined as $C_L(t) = 2L(t)/\rho cU^2(t)$, for two angles of attack $\alpha = 10^\circ$ and 30°. The dimensional lift is finite at $t = 0$, but the choice of using the instantaneous velocity $U(t)$ in the definition of C_L yields an infinite coefficient. Since $m \neq 0$, the added-mass force dominates at the initial instant and makes C_L infinitely positive as $t^{-(1+m)}$ rather than infinitely negative as $t^{-(m+2/3)}$. Also shown are the C_L from the viscous simulations (Re = 100) of Chen, Colonius, and Taira [14]. They plotted the "augmented lift coefficient" defined as C_L minus the added-mass component; here, we have reintroduced this component. There is good agreement early on with the rapid decrease from the infinite force at the initial instant. The model appears to capture an increase of C_L after the first minimum, which is associated with the LEV contribution to the effective bound circulation. However, this is noticeably different from that of the simulation data. The differences are likely to be Reynolds-number dependent, however, and we do not investigate this further here.

B. Regime II: Moderate-to-high angle of attack

Here, we assess the model for the higher angle of attack range given by (13) in Sec. IV. For a given m and η_α-J_o curve in the similarity space, the operators $\mathcal{F}_1$ and $\mathcal{F}_2$ in the vortex force (20) can be evaluated without any further input from the dimensional problem. For all computed cases we found that $\mathcal{F}_1(J_-T_- - J_+T_+) \ll \mathcal{F}_2(J_+N_+ + J_-N_-)$, by at least three orders of magnitude, while $\mathcal{F}_1(J_\pm T_\pm)$ and $\mathcal{F}_2(J_\pm N_\pm)$ are individually all of the same order (recall $\mathcal{F}_p$ is linear). This validates the statement made in Sec. III C that the tangential vortex force must be zero when $\Gamma_o = 0$ since then the plate only delivers a net normal impulse to the fluid. The tangential vortex force is not computed to be precisely zero because the similarity solutions at the LE and TE are obtained independent of each other. As such, the near mutual cancellation is a good first indication that the composite solution is accurately capturing the full vortex dynamics.

First, we make comparison to the viscous vortex particle method simulations (with Re = 1000) of Wang and Eldredge [7] for a flat plate that is impulsively accelerated $m = 0$ at $\alpha = 45^\circ$. The top row of Fig. 9 plots vorticity contours at several different "convective times" Ut/c; since $m = 0$, then Ut/c is also equal to the number of chords traveled. The bottom row of the figure plots the LE and TE vortex sheet positions from the current modeling of the same motion. There is good agreement early on with the size of the vortex spirals and core locations, at least up to one chord of travel. As expected, this begins to suffer as time increases, especially in the trailing-edge vortex sheet, which

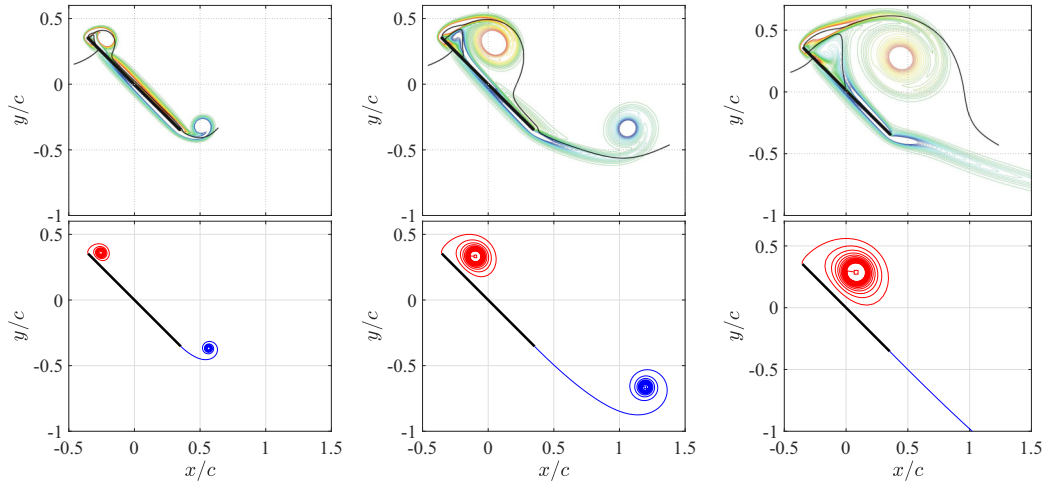

(a) $Ut/c = 0.24$ (b) $Ut/c = 1$ (c) $Ut/c = 2.24$

FIG. 9. Flow structure comparison for the case of impulsive acceleration $m = 0$ at $\alpha = 45^\circ$ at different convective times Ut/c as labeled. (Top) Vorticity contours from the viscous vortex particle method of Wang and Eldredge [7]. (Bottom) Vortex sheet positions predicted by the present theory. Since $m = 0$, then Ut/c is equal to the number of chords traveled.

does not "see" the downstream flow on the pressure side of the wing as the y/c position of the spiral core dips below the trailing edge. However, the farther this vortex spiral is from the plate, the less influence its exact position will have on the force experienced by the plate.

To this end, a better metric of the model performance is given by comparison of lift and drag coefficients C_L and C_D. For this purpose, we use the results of the high-fidelity Navier-Stokes simulations (with $\mathrm{Re} = 500$) from Darakananda and Eldredge [11]. The force coefficients are shown in Fig. 10 for two angles of attack: $\alpha = 45^\circ$ and 60°. The inviscid model of this paper provides a fair prediction up to $Ut/c \approx 2$ or about two chords of travel. Beyond this time, secondary vortex structures begin to form (see Figs. 4 and 11 of Ref. [11]) and the unsteady forces will begin to oscillate due to the periodic shedding of LE and TE vortices. The inviscid model, being the composite of two self-similar flows at the edges, will not explicitly capture this physics as the flow developments at the edges can no longer be considered independent and thus self-similar. More will be said about this limitation of the model in the following paragraphs.

Next, we consider the case of constant acceleration $m = 1$ and compare with the Navier-Stokes simulations of Pullin and Wang [1] for the flow around a thin elliptical airfoil; the elliptical cross section has a minor-to-major axis ratio $e = 0.125$. They provided numerical values of the physical parameters, but without specifying units: $c = 2$, $B = 4$. In effect, the time t can be taken in seconds and the fluid to be of unit density such that the Reynolds number is $\mathrm{Re} = Uc/\nu = 800$ at $t = 1$ s. We adhere to their specifications as well as their plotting of unscaled "dimensional" forces.

Figures 11(a)–11(d) plot the lift L and drag D as functions of time t from the viscous simulations of the elliptical airfoil for angles of attack $\alpha = 30^\circ$ and 60°. On each panel are vertical lines marking the times at which the airfoil has traveled 1, 2, 3, and 4 chord lengths. The forces exerted on the flat plate performing the same motions as modeled in this paper are also shown and exhibit rather good agreement at least to two chord lengths of travel. For lower α the trend is followed to almost $s/c = 3$ with some noticeable offset, while for higher α the quantitative match for $s/c < 2$ is much closer. The inertial force on the elliptical wing is due to the nonzero area of the body and it is worth noting that this is comparable to the *constant* added-mass force of the zero-thickness flat plate, which is quantified by the force values at $t = 0$ in the figure. As such, the vortex force does the

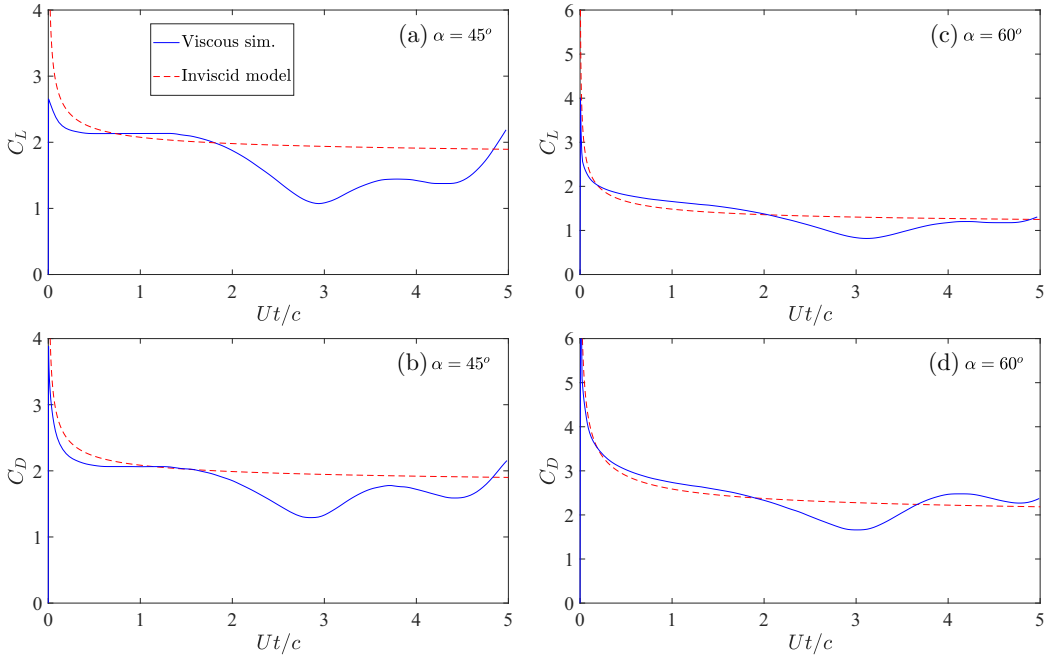

FIG. 10. Comparison of lift and drag coefficients vs Ut/c for cases with impulsive acceleration $m = 0$ at two angles of attack. (a), (b) C_L, C_D at $\alpha = 45^\circ$; (c), (d) C_L, C_D at $\alpha = 60^\circ$. The Navier-Stokes simulations are from Ref. [11]. The legend applies to all plots. Since $m = 0$ then Ut/c is equal to the number of chords traveled.

overwhelming majority of the predictive work in the inviscid model. Also plotted is the prediction from the single point vortex model of Pullin and Wang [1], which we recall contains no correction to the force due to asymmetry of the flow. We see that the current model provides a significant improvement in the prediction and can be attributed to the more effective representation of the vortex dynamics.

We note that the major deviation of the model from the simulations in Fig. 11 begins around the time of maximum lift. This corresponds to the first LEV shedding event. In other words, the vortex has grown so large that it can no longer remain attached to the plate and begins to convect downstream, thus giving a negative contribution to the lift. However, we can attempt to predict the initiation of this event, which we note is signaled by the arrival of the suction-side stagnation point, due to the reattached LE flow, at the trailing edge [32,36,37]. Figures 12(a) and 12(b) show the vortex sheet structures of the cases $\alpha = 30^\circ$ and 60° at the time of near maximum lift, which respectively occur at about $s/c = 3$ and 2 (Fig. 11). At the times of maximum lift we find that $\epsilon^2 \approx 1.1$ for each angle of attack case shown in Fig. 12. Recalling that $\epsilon^2 = R_v/c$ is a measure of the vortex spiral size relative to the plate chord, we might expect that $R_v \approx c$ is a good indication of the shedding event. Since the LE and TE flows are solved independent of each other, the composite stream function by superposition of the two flows is technically not valid; the streamlines do not have the visual character one would expect from a uniformly valid solution. However, at the times under consideration, the flow near the plate is dominated by the LEV sheet. Therefore, we estimate the suction-side stagnation point from the steam function of just this sheet. The stagnation streamlines are also plotted in Figs. 12(a) and 12(b). While the estimated stagnation point has not quite yet reached the trailing edge, we note that inclusion of the effect of the flow induced by the TEV sheet will act to bring the point closer to the edge. From this and the metric

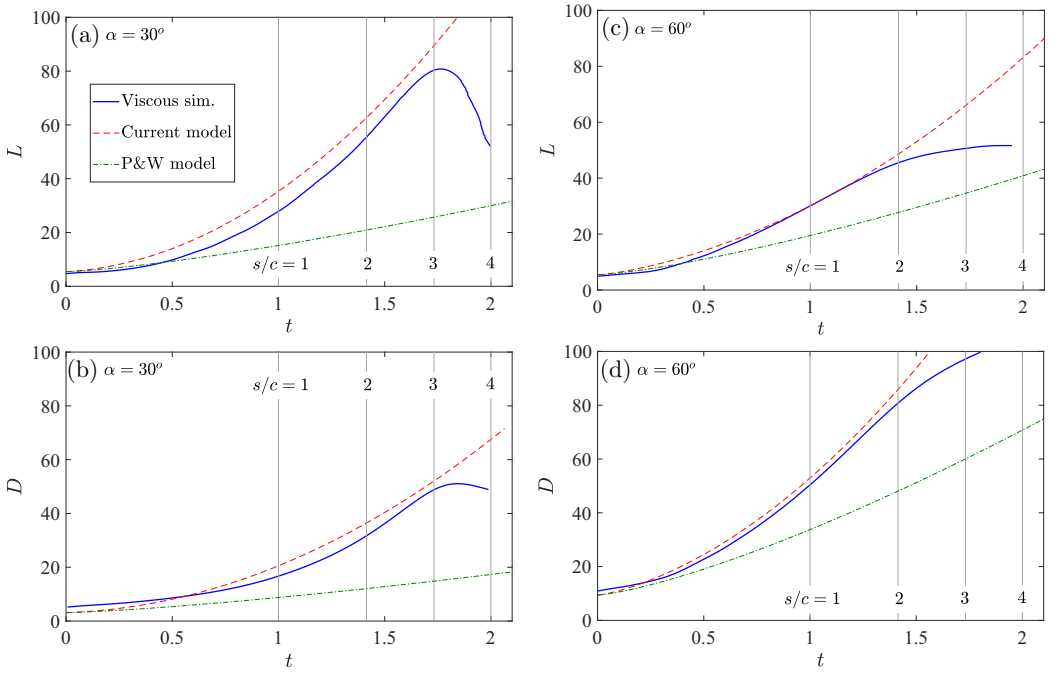

FIG. 11. Comparison of lift and drag forces vs t for cases with constant acceleration $m = 1$ at two angles of attack. (a), (b) L, D at $\alpha = 30^\circ$; (c), (d) L, D, at $\alpha = 60^\circ$. The Navier-Stokes simulations correspond to an ellipse of minor-to-major axis ratio $e = 0.125$ from Pullin and Wang [1]; their point vortex model is also shown and labeled as "P&W model." The legend applies to all plots. Vertical gray lines mark when the airfoil has traveled 1, 2, 3, and 4 chord lengths as labeled.

$R_v \approx c$, we conclude that the model provides an acceptable prediction of the initial LEV shedding event.

The results of Sec. VI indicate that the model is reasonably valid for a non-negligible distance and time traveled by the plate at different angles of attack and acceleration exponents. Hence, the

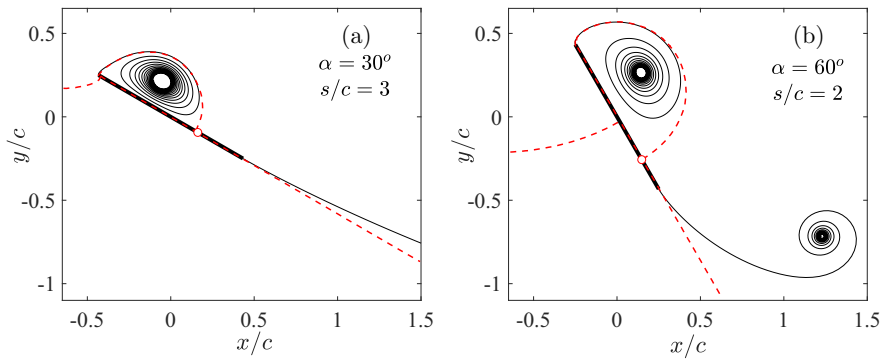

FIG. 12. The modeled vortex structure at the time of near maximum lift for the cases shown in Fig. 11. The stagnation streamline corresponding to the flow induced by just the LEV sheet is also plotted (dashed red lines). The corresponding suction-side stagnation point is marked by the circle symbol. (a) $\alpha = 30^\circ$, chords traveled: $s/c = 3$. The TE spiral is out of frame. (b) $\alpha = 60^\circ$, chords traveled: $s/c = 2$.

constraints in (12) do not appear to be too strict, and we have justified our ansatz of neglecting the integral term $\epsilon\{I_0(\omega) - I_1(\omega)\}$ from (10a).

VII. CONCLUDING REMARKS

In this paper we considered the canonical problem of a flat-plate airfoil accelerating in an inviscid fluid at a constant angle of attack. The objective was to extend the model of Pullin and Wang [1] to lower angles of attack and longer chords traveled. The full problem statement for the flat plate was approximated with self-similar solutions at both the leading and trailing edges. We expanded the attached outer flow to higher order rather than the sheet positions and circulations. As such, the attached flow contains a regular part representing the induction of distant effects, as well as the usual singular part necessitating the physical flow to separate at the sharp edge. It was shown that the higher-order regular part of the outer flow expansion corresponds to the sweeping component of the free-stream flow parallel to the plate. Moreover, we introduced a similarity variable that collapses the temporal growth of the vortex spiral length scale with the effect of angle of attack. Through this parameter the sweeping flow is brought into the same order as the singular flow. In other words, the effect of asymmetry is built in at the level of the governing equation.

The model was delineated into two angle of attack regimes. For the moderate-to-high range, the main assumption is that the development of the LEV and TEV structures remain independent of each other. Although the leading- and trailing-edge solutions are obtained independently, each is coupled to the sweeping flow in a simple manner. However, for the low-to-moderate range, the LEV and TEV developments can no longer be assumed independent because of the stronger sweeping component of the free stream. The LEV structure was represented by lumping its circulation with the plate-bound circulation into an effective bound circulation, which was then coupled to the governing equation for the evolution of the TEV structure.

Using this self-similar model, we constructed composite flow solutions in the physical domain that include the temporal variation of the length and circulation scalings as well as the implicit time dependence of the similarity variables. As a combined result, we were able to accurately capture a more complex evolution of the vortex structure, circulation dynamics, and forces exerted on the plate. The approximated flow is acceptably valid for the initial phase of the motion, up to about 2 to 3 chords of travel. This was corroborated by comparison with corresponding quantities obtained from Navier-Stokes simulations for both impulsive and constant accelerations and at different angles of attack.

Lastly, it is hoped that the two-tier model presented here could be used to complement the LESP concept and provide further insight to the initiation of flow separation at the leading edge. An ideal topic for future work would be identifying the state of the inviscid model at the Reynolds-number-dependent transition from attached to separated flow. Also, while we considered a constant angle of attack here, this does not prevent the application of the methodology to more general plate motions. For example, the modification of the complex potential to account for rotation is known and can be expanded to higher order in the same way as we have done for the translational component of the attached outer flow.

ACKNOWLEDGMENTS

We acknowledge the partial support of the National Science Foundation (NSF) and Office of Naval Research (ONR) in this work. We also thank the anonymous reviewers whose comments helped improve the quality of the manuscript.

APPENDIX: SINGLE POINT VORTEX MODEL

Here, the solution to the point vortex approximation of (13) and (14) is given. The point vortex solution with $\eta_\alpha = 0$ and $J_o = 0$ corresponding to the semi-infinite plate was originally given by

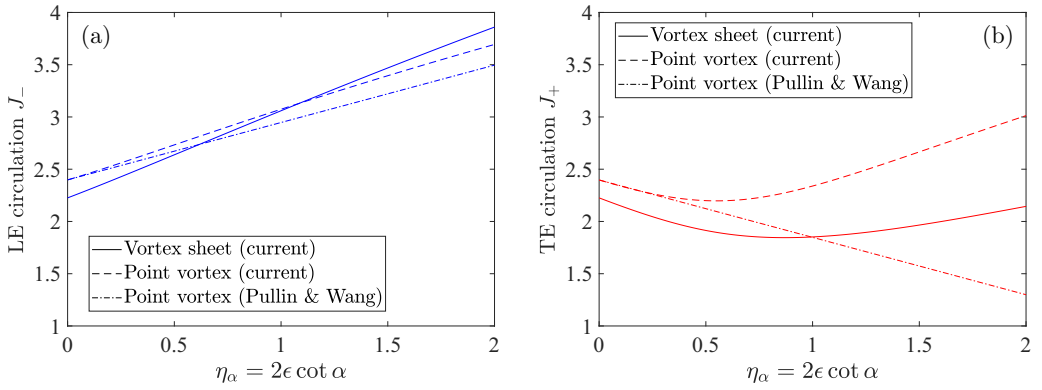

FIG. 13. Comparison of the nondimensional circulations as predicted by the vortex sheet and point vortex models of this study, along with the point vortex model of Pullin and Wang [1]. The parameters are $m = 1$ (constant acceleration) and $J_o = 0$. (a) Leading-edge circulation J_-. (b) Trailing-edge circulation J_+.

Rott [38]. Pullin and Wang [1] derived a similar model for their perturbation series, in which Rott's model is the leading-order term. Here, we follow suit and obtain the point vortex solution for $\eta_\alpha \neq 0$ and $J_o \neq 0$.

Equation (10a) is a special case for flow around a flat plate. For generality, we consider the case for a wedge of arbitrary internal angle $\beta\pi = (2 - 1/n)\pi$; recall the outer-flow expansion in (1) and (2). The corresponding equations are readily obtained by replacing all $\frac{1}{2}$ powers in (13) and (14) with n and also putting $C_o = (1 - n)$. The point vortex approximation of the governing equations is (e.g., see DeVoria and Mohseni [22])

$$(1-n)[\overline{\omega}_{\pm v} + Q\overline{\omega}_{\pm v}] = n\omega_{\pm v}^{n-1}\left\{-i(1 \pm J_o) \pm \eta_\alpha \omega_{\pm v}^n - \frac{J_\pm}{2\pi i}\left[\frac{1}{\omega_{\pm v}^n + \overline{\omega}_{\pm v}^n} + \frac{1-n}{2n\omega_{\pm v}^n}\right]\right\}, \tag{A1}$$

$$0 = (1 \pm J_o) - \frac{J_\pm}{2\pi}\left[\frac{1}{\omega_{\pm v}^n} + \frac{1}{\overline{\omega}_{\pm v}^n}\right], \tag{A2}$$

where $\omega_{\pm v} = R_\pm e^{i\theta_\pm}$ are the TE (+) and LE (−) point vortex locations in similarity space. For a given vortex, the above are three equations for the three unknowns $J_\pm$, $R_\pm$, and $\theta_\pm$. After some algebra these can be reduced to

$$0 = \left[1 + \frac{1}{4n\cos^2(n\theta_\pm)}\right] \pm \frac{2\eta_\alpha R_\pm^n \sin(n\theta_\pm)}{(1 \pm J_o)}, \tag{A3}$$

$$0 = (1-n)(1+Q) - nR_\pm^{n-2}\left[\frac{(1 \pm J_o)(1-n)\sin(n\theta_\pm)}{4n\cos^2(n\theta_\pm)} \pm \eta_\alpha R_\pm^n\right], \tag{A4}$$

$$0 = \frac{J_\pm}{2\pi} - \frac{(1 \pm J_o)R_\pm^n}{2\cos(n\theta_\pm)}. \tag{A5}$$

When $\eta_\alpha = 0$ the above can be further manipulated to obtain a closed-form solution, which returns Rott's solution when $J_o = 0$. Although a numerical solution is required for $\eta_\alpha \neq 0$, the system is quite simple. Again, $n = \frac{1}{2}$ corresponds to the flat plate. Once the system has been solved for desired ranges of η_α and J_o, the point vortex force could be obtained from (20) with the approximations $N_\pm \approx \mathrm{Re}\{\sqrt{\omega_{\pm v}}\}$ and $T_\pm \approx \mathrm{Im}\{\omega_{\pm v}\}$.

Figures 13(a) and 13(b) show an example of the LE and TE nondimensional circulations J_- and J_+, respectively, as predicted by the current point vortex model. The particular case corresponds to constant acceleration $m = 1$ and $J_o = 0$. For comparison, the predictions from our full vortex sheet model and the point vortex model of Pullin and Wang [1] are also shown. The model of Pullin and

Wang [1] is a linearization at $\eta_\alpha = 0$,

$$J_\pm \approx J_0 \mp \left(\frac{\partial J_\pm}{\partial \eta_\alpha}\right)\eta_\alpha = J_0 \mp \epsilon J_1, \tag{A6}$$

whereas the current point vortex model maintains the nonlinear behavior with η_α. The expression for the quantity $J_1 = 2(\partial_{\eta_\alpha} J_\pm)\cot\alpha \geqslant 0$ obtained by Pullin and Wang is given in their Eq. (3.27). For small η_α there is an offset of both point vortex models from the vortex sheet, which is the result of concentrating all circulation at a single point.

[1] D. I. Pullin and Z. J. Wang, Unsteady forces on an accelerating plate and application to hovering insect flight, J. Fluid Mech. **509**, 1 (2004).

[2] J. Katz, A discrete vortex method for the non-steady separated flow over an airfoil, J. Fluid Mech. **102**, 315 (1981).

[3] J. M. R. Graham, The lift on an aerofoil in starting flow, J. Fluid Mech. **133**, 413 (1983).

[4] M. A. Jones, The separated flow of an inviscid fluid around a moving flat plate, J. Fluid Mech. **496**, 405 (2003).

[5] S. Michelin and S. G. Llewellyn-Smith, An unsteady point vortex method for coupled fluid-solid problems, Theor. Comput. Fluid Dyn. **23**, 127 (2009).

[6] X. Xia and K. Mohseni, Lift evaluation of a two-dimensional pitching flat plate, Phys. Fluids **25**, 091901 (2013).

[7] C. Wang and J. D. Eldredge, Low-order phenomenological modeling of leading-edge vortex formation, Theor. Comput. Fluid Dyn. **27**, 577 (2013).

[8] J. Li and Z. Wu, A vortex force study for a flat plate at high angle of attack, J. Fluid Mech. **801**, 222 (2016).

[9] X. Xia and K. Mohseni, Unsteady aerodynamics and vortex-sheet formation of a two-dimensional airfoil, J. Fluid Mech. **830**, 439 (2017).

[10] D. Darakananda, A. F. de Castro da Silva, T. Colonius, and J. D. Eldredge, Data-assimilated low-order vortex modeling of separated flows, Phys. Rev. Fluids **3**, 124701 (2018).

[11] D. Darakananda and J. D. Eldredge, A versatile taxonomy of low-dimensional vortex models for unsteady aerodynamics, J. Fluid Mech. **858**, 917 (2019).

[12] S.-I. Sohn, An inviscid model of unsteady separated vortical flow for a moving plate, Theor. Comput. Fluid Dyn. **34**, 187 (2020).

[13] D. I. Pullin, The large-scale structure of unsteady self-similar rolled-up vortex sheets, J. Fluid Mech. **88**, 401 (1978).

[14] K. Chen, T. Colonius, and K. Taira, The leading-edge vortex and quasisteady vortex shedding on an accelerating plate, Phys. Fluids **22**, 033601 (2010).

[15] S. A. Ansari, R. Żbikowski, and K. Knowles, Non-linear unsteady aerodynamic model for insect-like flapping wings in the hover. Part 2: Implementation and validation, Proc. Inst. Mech. Eng., Part G **220**, 169 (2006).

[16] K. Ramesh, A. Gopalarathnam, K. Granlund, M. V. Ol, and J. R. Edwards, Discrete-vortex method with novel shedding criterion for unsteady aerofoil flows with intermittent leading-edge vortex shedding, J. Fluid Mech. **751**, 500 (2014).

[17] Y. Hirato, M. Shen, A. Gopalarathnam, and J. R. Edwards, Flow criticality governs leading-edge-vortex initiaition on finite wings in unsteady flow, J. Fluid Mech. **910**, A1 (2021).

[18] A. R. Jones and J. D. Eldredge, Leading-edge vortices: Mechanics and modeling, Annu. Rev. Fluid Mech. **51**, 75 (2019).

[19] G. F. Carrier, M. Krook, and C. E. Pearson, *Functions of a Complex Variable: Theory and Technique*, 1st ed. (McGraw-Hill, New York, 1966).

[20] H. K. Moffatt, Viscous and resistive eddies near a sharp corner, J. Fluid Mech. **18**, 1 (1964).

[21] P. Zhang and K. Mohseni, Dipole model of vorticity at the moving contact line, Int. J. Multiphase Flow **103**, 169 (2018).
[22] A. C. DeVoria and K. Mohseni, New insights from inviscid modeling of starting flow separation with roll-up, J. Fluid Mech. **903**, A24 (2020).
[23] A. C. DeVoria and K. Mohseni, The vortex-entrainment sheet in an inviscid fluid: Theory and separation at a sharp edge, J. Fluid Mech. **866**, 660 (2019).
[24] E. J. Townsend, *Functions of a Complex Variable*, 1st ed. (Henry Holy and Company, New York, 1942).
[25] R. V. Churchill, *Complex Variables and Applications*, 1st ed. (McGraw-Hill, New York, 1948).
[26] L. M. Milne-Thomson, *Theoretical Hydrodynamics* (Macmillan Education, London, 1968).
[27] J. Newman, *Marine Hydrodynamics* (MIT Press, Cambridge, MA, 1977).
[28] G. K. Batchelor, *An Introduction to Fluid Dynamics* (Cambridge University Press, Cambridge, UK, 1967), pp. 406–407.
[29] C. S. Yih, *Fluid Mechanics: A Concise Introduction to the Theory*, 1st ed. (McGraw-Hill, New York, 1966).
[30] P. G. Saffman, *Vortex Dynamics* (Cambridge University Press, Cambridge, UK, 1992).
[31] C. P. Ellington, The aerodynamics of hovering insect flight. IV. Aerodynamic mechanisms, Philos. Trans. R. Soc. London B **305**, 79 (1984).
[32] A. C. DeVoria and K. Mohseni, On the mechanism of high-incidence lift generation for steadily translating low-aspect-ratio wings, J. Fluid Mech. **813**, 110 (2017).
[33] H. Wagner, Über die Entstehung des dynamischen Auftriebes von Tragflügeln, J. Appl. Math. Mech. **5**, 17 (1925).
[34] J. Li and Z. Wu, Unsteady lift for the Wagner problem in the presence of additional leading/trailing edge vortices, J. Fluid Mech. **769**, 182 (2015).
[35] E. C. Polhamus, Predictions of vortex-lift characteristics using a leading-edge suction analogy, J. Aircraft **8**, 193 (1971).
[36] D. Lipinski, B. Cardwell, and K. Mohseni, A Lagrangian analysis of a two-dimensional airfoil with vortex shedding, J. Phys. A: Math. Theor. **41**, 344011 (2008).
[37] D. E. Rival, J. Kriegseis, P. Schuab, A. Widmann, and C. Tropea, Characteristic length scales for vortex detachment on plunging profiles with varying leading-edge geometry, Exp. Fluids **55**, 1660 (2014).
[38] N. Rott, Diffraction of a weak shock with vortex generation, J. Fluid Mech. **1**, 111 (1956).